Heat Capacity and Anisotropic Thermal Conductivity in Cr$_2$AlC Single Crystals at High Temperature

A. Champagne,* J.-L. Battaglia, T. Ouisse, F. Ricci, A. Kusiak, C. Pradere, V. Natu, A. Dewandre, M. J. Verstraete, M. W. Barsoum, and J.-C. Charlier

ACCESS | 📊 Metrics & More | 📄 Article Recommendations | 🆂🅸 Supporting Information

ABSTRACT: The temperature dependences of both heat capacity and thermal conductivity in nanolamellar Cr$_2$AlC single crystals are measured using modulated photothermal radiometry and compared to first-principles calculations. The electronic contribution to the thermal conductivity of Cr$_2$AlC single crystals is computed *ab initio* by determining the electronic transport coefficients using density functional theory and by solving the Bloch−Boltzmann transport equation with a temperature-dependent relaxation time. The lattice thermal conductivity is predicted by going beyond the quasi-harmonic approximation and considering renormalized second- and third-order force constant matrices, with anharmonic three-phonon scattering, isotopic scattering, and scattering by carbon vacancies. Isotopic scattering does not modify the lattice thermal conductivity. In contrast, even a small concentration of carbon vacancies induces a substantial decrease of the in-plane lattice thermal conductivity. The anisotropy measured in the thermal conductivity, with a ratio of ~2 over the whole temperature range, is confirmed theoretically. This anisotropy seems to mainly arise from lattice contributions. A similar anisotropy is expected for other MAX phases with identical layered structures.
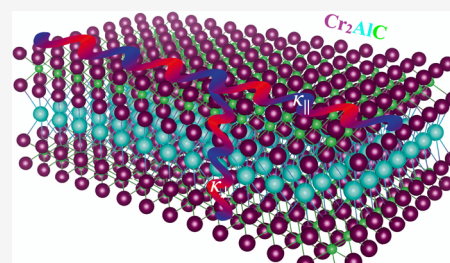
1. INTRODUCTION

MAX phases are layered, hexagonal, early-transition metal carbides and nitrides with the formula $M_{n+1}AX_n$, where M represents an early transition metal, A an element from groups 13 to 16, X either carbon or nitrogen, and n varies from 1 to 3. There are currently more than 150 MAX phases known,[1,2] including both quaternary in- and out-of-plane ordered phases,[3−5] as well as the recently discovered rare-earth-containing MAX phases.[6−8] In contrast to graphite-like layered materials, MAX phases combine strong intralayer covalent/metallic MX bonds and weaker interlayer metallic MA bonds. In most cases, atomic masses are very different—C atoms are light in comparison with the M and A atoms—leading to a wide range of optical phonon energies.[9] By now, it is well established that at least a subset of MAX phases combine some of the best properties of metals and ceramics,[1,9,10] including high electrical and thermal conductivities, chemical, oxidation, and thermal shock resistances, as well as reversible deformation[11] and bulk ripplocations.[12−16] The growing interest of the scientific community results both from their own intrinsic physical properties and from the possibility to exfoliate them to form a new family of two-dimensional materials, called MXenes.[17] Taken together, these characteristics give MAX phases their anisotropic properties. Pure MAX phases were synthesized for the first time in 1996,[18] but the lack of large single crystals has long prohibited a direct assessment of the anisotropy of the physical properties expected from their crystal structure (see Figure 1). As a
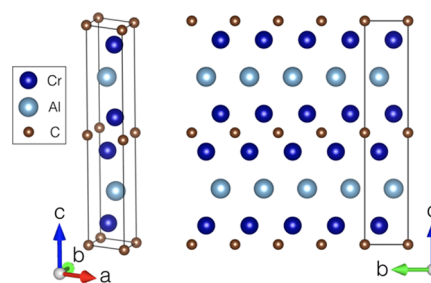

**Figure 1.** Atomic structure of Cr$_2$AlC ($P6_3/mmc$ space group, $a = b = 0.286$ nm and $c = 1.282$ nm).

consequence, most of the studies on the electrical and thermal transport in MAX phases were performed on polycrystals.[19,20] Since 2011, macroscopic single crystals have been available,[21−24] and their magneto-transport properties have been investigated,[25,26] as well as their electronic structure[27] and elastic properties.[16]

Recently, the phonon dispersion branches of Cr$_2$AlC MAX phase single crystals have been obtained experimentally with
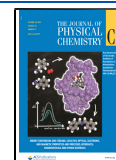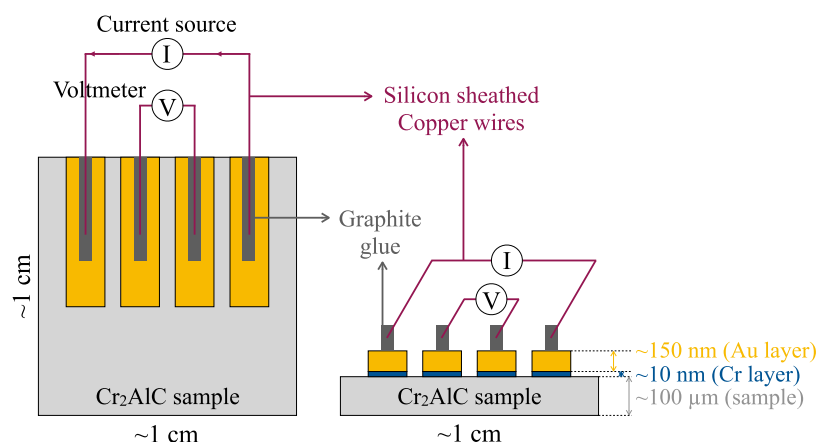
Figure 2. Schematic of the in-plane resistivity measurements in Cr_2AlC using a four-probe configuration with equidistant and parallel pads.

neutron inelastic scattering and computed *ab initio* using the density functional perturbation theory (DFPT).[28] The anisotropy of the phonon branches has been predicted with a very satisfactory accuracy when compared to experiment, thus allowing for further investigation of the anisotropy of the thermal conductivity in these MAX single crystals.

In this work, the heat capacity and the anisotropic thermal conductivity of Cr_2AlC single crystals are measured from room temperature (RT) up to 600°C. The experimental techniques are described in Sections 2.1 and 2.2 and the results are discussed in Section 3.1. The measurements are compared to *ab initio* calculations and to fundamental analytic models, including the Wiedemann−Franz law and the Callaway and Klemens models. The electronic and lattice contributions to the thermal conductivity are computed using the BoltzTraP2 code[29,30] and the temperature-dependent effective potential (TDEP) code,[31−33] respectively. Computational details can be found in Section 2.3. The theoretical predictions are presented in Section 3.2, and all results are discussed in Section 4. Finally, conclusions are drawn in Section 5.

2. METHODS

2.1. Crystal Growth. Single crystalline platelets of Cr_2AlC are grown from a liquid solution of composition $x_{Cr} = 0.36$, $x_{Al} = 0.57$, and $x_C = 0.07$. After a temperature plateau at $T_{max} = 1650$ °C for 2 h to ensure carbon dissolution, crystal growth is achieved by slowly cooling the solution from T_{max} down to $T = 1200$°C during time periods ranging from 5 to 7 days with an Ar pressure $p_{Ar} = 1.5$ bar. Slow cooling aims at limiting unwanted spontaneous nucleation by putting to good use Ostwald ripening. The growth rate is much slower along the *c*-axis, resulting in a morphology with a low aspect ratio. The largest platelet areas are around 6−10 cm^2 with thicknesses limited to 2 mm. Single crystals are cleaved and do not include grain boundaries. The crystal quality is checked by X-ray Laue transmission and through neutron diffraction. More details on the sample preparation and on their structure can be found in ref 28.

2.2. Electrical and Thermal Conductivity Measurements. Cr_2AlC single crystals are first cut with a diamond wire saw to obtain square-shaped samples of about 1−2 cm^2. They are then polished to obtain a uniform thickness of about 100 μm.

Four equidistant and parallel Cr/Au contact pads are deposited on the single crystals, as illustrated in Figure 2.

The initial Cr layer is 10 nm thick followed by a ∼150 nm thick gold layer. Later, silica sheathed copper wires are attached to the gold pads using graphite glue (Ted Pella). The whole assembly is placed inside a furnace under flowing Ar and the furnace is heated up to 700 °C at 5 °C min^{-1}. The copper wire contacts coming out of the furnace are passed through a rubber stopper to protect the inert atmosphere inside. A 100 mA current is passed through the outer wires using a constant current source (Hewlett-Packard, DC current source) and the voltage at the inner probes is recorded using a voltmeter (Keithley Instruments). The correction factor used to correct the raw resistance data is a function of the sample geometry and is calculated according to ref 34.

The temperature dependence of the heat capacity is obtained using the differential scanning calorimetry (DSC) technique in the RT−600 °C temperature range, with a heating rate of 10 °C min^{-1}.

Both in-plane and out-of-plane thermal conductivities of the Cr_2AlC samples are measured using the modulated photo-thermal radiometry (MPTR) within two distinct frequency ranges.[35] The characterization is performed in the RT−600 °C temperature range under Ar gas flow. The MPTR method consists in subjecting the sample's surface to a periodic heat flux generated by a modulated laser. The increase in temperature leads to modulated infrared (IR) radiation, which is monitored using a HgCdTe IR detector. The amplitude and the phase are given using a lock-in amplifier. In addition, the in-plane thermal diffusivity at RT is measured using the pulsed flying spot (PFS) with the logarithmic parabolas method.[36] The out-of-plane thermal diffusivity at RT is also measured using the periodic pulse radiometry technique (PPRT),[37] which consists of heating the front face of the sample using a periodic laser pulse and measuring the transient average temperature on the rear face using an IR detector. Similar to the MPTR method, thermal diffusivity is identified by minimizing the quadratic gap between the experimental relative change in the temperature and the one calculated from a model of the heat transfer within the PPRT experimental configuration. The minimization is performed using the Levenberg−Marquardt algorithm.

2.3. First-Principles Computational Modeling. The structural, electronic, and vibrational properties are computed *ab initio* using the density functional theory (DFT)[38,39] and density functional perturbation theory (DFPT),[40−44] respectively, using the ABINIT package,[45−47] which is based on plane-
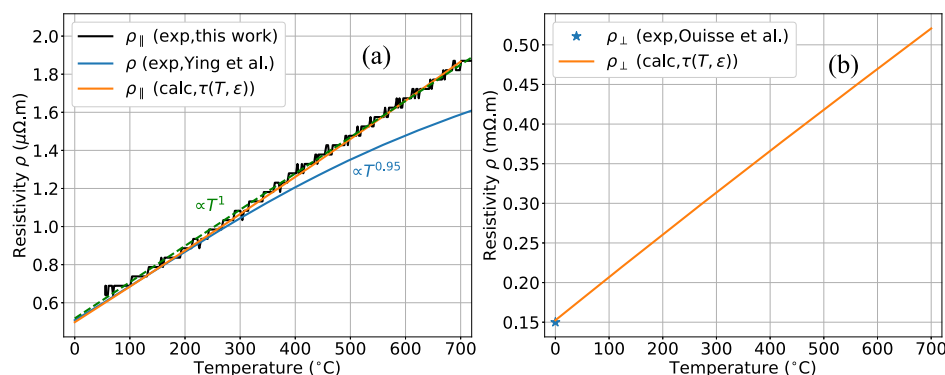
Figure 3. (a) Temperature-dependence measurements of the in-plane resistivity $\rho_\parallel$ for Cr_2AlC single crystals (black line), compared to the experimental data from ref 51 for a polycrystalline sample (blue line) and to the computed in-plane resistivity (orange line) using the relaxation time $\tau(T, \varepsilon)$ as defined in eq 15. The dashed green line is a guide to the eye, highlighting the linear temperature dependence of the resistivity. (b) Predicted out-of-plane resistivity (orange line) using $\tau(T, \varepsilon)$, compared to the experimental data from ref 25.
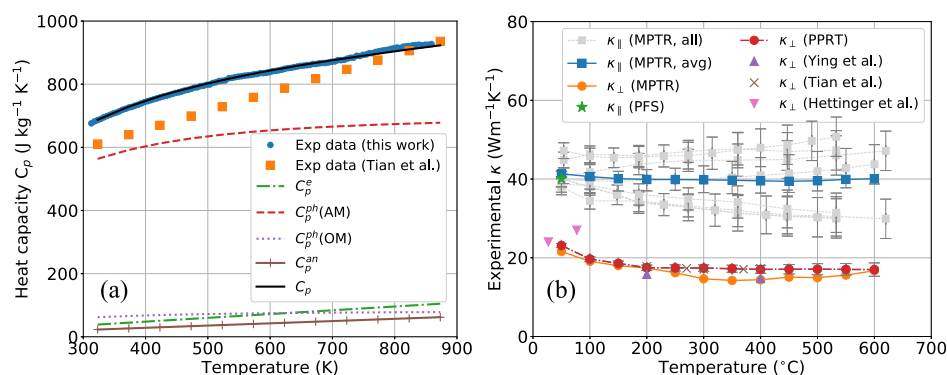

Figure 4. (a) Heat capacity measurements of Cr_2AlC single crystals measured experimentally (blue dots), compared to the experimental data from ref 52 (orange squares) and theoretical values (black solid line) obtained from electrons (C_p^e), acoustic and optical phonons [$C_p^{ph}(AM)$, $C_p^{ph}(OM)$], and anharmonic (C_p^{an}) contributions. (b) Measured in-plane ($\kappa_\parallel$) and out-of-plane ($\kappa_\perp$) thermal conductivities using various techniques, compared to the values found in the literature.[20,51,52] Error bars for MPTR and PPRT measurements are represented by dark gray lines.

wave basis sets to represent the Kohn–Sham orbitals and charge density. The exchange–correlation functional is approximated using the generalized gradient approximation as proposed by Perdew, Burke, and Ernzerhof.[48] Optimized norm-conserving Vanderbilt pseudopotentials[49] are used to describe the core-valence interaction. A plane-wave kinetic energy cutoff of 40 Hartree is determined through a careful convergence investigation. The first Brillouin zone is sampled with an $18 \times 18 \times 6$ Monkhorst-Pack k-point grid, and a Gaussian smearing of 1 mHa is used to accelerate the convergence. Both Fermi surfaces and Fermi velocities are obtained on a dense homogeneous $72 \times 72 \times 72$ k-point grid and are visualized using the Fermisurfer code.[50] The optimization of the cell parameters leads to an underestimation of the experimental values and thus to an overestimation of the high-frequency phonon modes, which is problematic in the study of transport properties. Following our previous work,[28] the lattice parameters are thus kept fixed at the experimental values for Cr_2AlC $a = 0.286$ nm and $c = 1.282$ nm, and the atomic positions inside the unit cell are fully optimized until the largest force is smaller than 2.5×10^{-4} eV Å^{-1}.

The thermal conductivity can be decomposed into its electronic and lattice contributions, such that $\kappa = \kappa_e + \kappa_l$. The transport theory for electrons is implemented in the Boltz-TraP2 code,[29,30] which computes the electronic transport coefficients assuming rigid bands (unchanged either with doping or with temperature) and usually a constant relaxation

time τ_0. The estimation of the lattice contribution includes anharmonic processes and, hence, the computation of the third-order force constant matrix. The effective second- and third-order interatomic force constants (IFCs) are obtained at a given temperature from a fit of DFT forces in supercells with thermally displaced atoms (based on initial DFPT harmonic estimates) using the TDEP code.[31−33] The lattice thermal conductivity tensor and cumulative thermal conductivity are then obtained from the iterative solution of the phonon Bolzmann transport equation (BTE). External scattering processes are also considered, i.e., vacancy, isotope, and grain boundary scattering processes. The isotopic concentrations are chosen to be as close as possible to the natural ones: carbon of 98.93% ^{12}C, 1.07% ^{13}C, aluminum of 100% ^{27}Al, and chromium of 4.35% ^{50}Cr, 83.79% ^{52}Cr, 9.50% ^{53}Cr, and 2.36% ^{54}Cr. The determination of the phonon scattering rates due to three-phonon collisions and extrinsic scattering processes using an *ab initio* approach is described in detail in refs 31−33.

3. RESULTS

3.1. Measurements. *3.1.1. Electrical Resistivity.* To gain insight into the transport properties of Cr_2AlC single crystals, the in-plane electrical resistivity $\rho_\parallel(T)$ is measured experimentally, in the 50−750 °C temperature range, using a four-probe configuration as the one depicted in Figure 2. The result is depicted in Figure 3a. Not surprisingly, a linear temperature

dependence is observed, as is usual in metals, due to the linear increase of the phonon occupation with temperature. This experimental curve will be further used to investigate the thermal transport in Cr_2AlC single crystals in Section 3.2.2. A value of ~0.7 $\mu\Omega$ m is obtained at 50 °C, which is about 10 times higher than the one previously measured by Ouisse et al.[25] This might be due to the configuration used to measure the resistivity, where the contacts are all deposited on the top surface. On the other hand, it appears that the curve is close to previous reports for Cr_2AlC polycrystals with electrical resistivities ranging from 0.6 to 0.74 $\mu\Omega$m at 300 K.[20,51,52] It can be noted here that the electrical resistivity of Cr_2AlC is almost twice higher than the one of other M_2AlC systems.[9] For example, the electrical resistivities of Ti_2AlC,[53] V_2AlC,[20] and Nb_2AlC[20] are 0.36, 0.25, and 0.29 $\mu\Omega$m, respectively, at 300 K.

3.1.2. Heat Capacity and Thermal Conductivity. Both in-plane and out-of-plane thermal conductivities are measured using the MPTR technique with two distinct frequency ranges. At a high (low) frequency, the measured phase is sensitive to the in-plane (out-of-plane) thermal diffusivity $a_{\parallel}$ ($a_{\perp}$). Using the measured density $\rho = 5210$ kg m^{-3} and the temperature-dependent heat capacity $C_p(T)$ (see Figure 4a), the temperature-dependent in-plane thermal conductivity $\kappa_{\parallel}(T)$ and out-of-plane thermal conductivity $\kappa_{\perp}(T)$ are obtained. $\kappa_{\parallel}(T)$ measured on several Cr_2AlC samples using the MPTR are depicted in gray in Figure 4b. A total of seven curves are reported among which four increase with T at high temperatures and three decrease with T at high temperatures. The deviations between the different gray curves may result from the variable quality of the different samples and the sensitivity of the measurements. They still provide results in the same order of magnitude, with the average thermal conductivity curve depicted in blue in the same figure. The out-of-plane thermal conductivity $\kappa_{\perp}(T)$ of a unique sample is measured and depicted in orange in Figure 4b. Values of $\kappa_{\parallel} = 41.3$ Wm^{-1} K^{-1} and $\kappa_{\perp} = 21.6$ Wm^{-1} K^{-1} are obtained at RT.

In addition, the in-plane thermal diffusivity at RT is measured using the PFS with the logarithmic parabolas method.[36] A value of $a_{\parallel} = 11.4$ mm^2 s^{-1} is measured, leading to a $\kappa_{\parallel} = 40.8$ Wm^{-1} K^{-1} at RT. This PFS measurement is useful to validate the MPTR values. The temperature dependence of $\kappa_{\perp}$ is also measured using the PPRT technique and the results are reported in Figure 4b. These values confirm rather well those obtained with the MPTR technique, although the slight increase at the highest temperatures is not observed anymore. Given the high standard deviation on $\kappa_{\perp}$ using the MPTR technique, we suspect the increase is spurious. Comparisons with values of $\kappa_{\perp}$ in the literature are also reported in Figure 4b. The measurements obtained by Tian et al.[52] in a more narrow temperature range fit rather well with the present measurements. As a global observation, the in-plane thermal conductivity is found to be almost constant in the whole temperature range, whereas the out-of-plane thermal conductivity slightly decreases with increasing temperature and before saturation above 200 °C. As importantly, an anisotropy ratio of about 2 is found over the whole temperature range.

3.2. Theoretical Simulations. *3.2.1. Heat Capacity.* The total heat capacity C_p is composed of several contributions, including the electronic part (from the metallic character of Cr_2AlC), the lattice part, and the anharmonic scattering that occurs at a high temperature[59]

$$C_p = C_p^e + C_p^{ph} + C_p^{an} \tag{1}$$

where

$$C_p^e = \frac{\pi^2 k_B^2 N(E_F)}{3 q_e N_A} T \tag{2}$$

is the electronic contribution with $N(E_F)$ denoting the density of states (DOS) at the Fermi energy E_F. The phonon contribution $C_p^{ph} = C_p^{ph}(AM) + C_p^{ph}(OM)$ is accounted with both the acoustic modes (AM) and the optical modes (OM). Assuming all of the atoms are involved equally within the AM, the contribution of AM is conventionally expressed from the phonon DOS $D_p(\omega)$ given, within the Debye approximation, by

$$D_p(\omega) = \frac{\omega^2}{2\pi^2 v^3} \tag{3}$$

with

$$v = 3^{1/3} \left(\frac{1}{v_L^3} + \frac{2}{v_T^3} \right)^{-1/3} \tag{4}$$

the sound velocity, as

$$C_p^{ph}(AM) = \frac{\hbar^2}{k_B T^2} \int_0^{\omega_D} \frac{\omega^2 e^{\hbar\omega/k_B T}}{(e^{\hbar\omega/k_B T} - 1)^2} D_p(\omega) d\omega \tag{5}$$

$$= 9 N k_B \frac{T^3}{\Theta_D^3} \int_0^{\omega_D} \frac{\hbar^5 \omega^4 e^{\hbar\omega/k_B T}}{k_B^5 T^5 (e^{\hbar\omega/k_B T} - 1)^2} d\omega \tag{6}$$

In this relationship, $\hbar$ is the reduced Planck constant, k_B the Boltzmann constant, Θ_D the Debye temperature, and $N = \int_0^\infty D_p(\omega) d\omega$. Assuming all of the phonons are involved in the high-temperature range, $N = \frac{4 N_A}{M}$, where $M = 2 M_{Cr} + M_{Al} + M_C$ is the total molar mass. Using the Debye approximation, it comes to $N = \frac{V_0 \omega_D^3}{6\pi^3 v^3}$, where V_0 is the volume of the elementary cell. In addition, the Debye temperature $\Theta_D = \frac{\hbar \omega_D}{k_B} = \frac{\hbar (6 N \pi^2 v^3)^{1/3}}{k_B}$ is found to be 675 K, which is the value frequently reported in the literature.[58] The heat capacity related to optical modes is estimated using the Einstein model as

$$C_p^{ph}(OM) = \frac{3 N k_B \Theta_E^2 e^{\Theta_E/T}}{T^2 (e^{\Theta_E/T} - 1)^2} \tag{7}$$

where $\Theta_E = \frac{\hbar \omega_E}{k_B}$ is the Einstein temperature. Finally, at a high temperature, anharmonic effects can also be taken into account as a contribution to the heat capacity using

$$C_p^{an} = \frac{9 N_A \alpha_V^2 B V_0 T}{M} \tag{8}$$

where B is the bulk modulus and α_V the thermal expansion coefficient.

The total heat capacity distributed among its various contributions (electrons, phonons, and anharmonic processes − thermal expansion) and computed using the data reported in Table 1 is presented in Figure 4a by a black line that overlaps the experimental results in blue.

3.2.2. Electronic Thermal Conductivity. 3.2.2.1. Wiedemann−Franz Law. As a first approximation, the electronic

Table 1. Theoretical and Experimental Values Used to Model the Heat Capacity and the Thermal Conductivity of the Cr$_2$AlC MAX Phase

Cr$_2$AlC	parameter description(s)	value(s)	refs
M [g mol^{-1}]	molar mass	52(Cr)/27(Al)/12(C)	
a [Å] – c [Å]	lattice constants	2.863–12.814	exp 54–56.
V_0 [Å^3]	volume of the elementary cell	90.6	exp 54, 55.
ρ [kg m^{-3}]	density	5210	exp.
L [cm]	grain size (@300 K)	~1–2	this work
α_V [K^{-1}]	thermal expansion coefficient	11.2 × 10^{-6}	exp 56, 57.
B [GPa]	bulk modulus	226	calc 54, 55, 57, 58.
Θ_E [K]	Einstein temperature	260, 320, 925	exp 19.
Θ_D [K]	Debye temperature	675	this work
γ [J mol^{-1} K^{-2}]	temperature coeff. of C_p^e	17.15 × 10^{-3}	exp 19.
G	Grüneisen parameter (=$3B\alpha_V/C_P$)	1.5	calc 56.
v_{T_1}/v_{T_2} [m s^{-1}]	transverse sound velocities along		
	Γ−M	4820/5216	calc 28.
	Γ−K	4820/5216	calc 28.
	Γ−A	5056/5056	calc 28.
v_L [m s^{-1}]	longitudinal sound velocity along		
	Γ−M	7664	calc 28.
	Γ−K	7664	calc 28.
	Γ−A	9566	calc 28.
$N(E_F)$ [(eV unit cell)$^{-1}$]	density of states at the Fermi level	6.46	exp 58.
E_F (eV)	Fermi energy	8.07	calc 55.

contribution to the thermal conductivity κ_e can be quickly estimated using the Wiedemann–Franz law as

$$\kappa_e = \frac{L_0 T}{\rho(T)} \tag{9}$$

In this relationship, $L_0 = 2.45 \times 10^{-8}$ WΩ K^{-2} is the Lorentz number and $\rho(T)$ is the temperature-dependent electrical resistivity. The experimental in-plane electrical resistivity $\rho_\parallel(T)$ depicted in Figure 3a is used to compute the in-plane electronic thermal conductivity $\kappa_e^\parallel$. As expected from the quasi-linear temperature dependence of the resistivity, an almost temperature-independent electronic thermal conductivity is observed in Figure 5a.

3.2.2.2. Boltzmann Transport Equation. From first principles, the electronic contribution to the thermal conductivity κ_e can be obtained by solving the BTE for electrons. The BTE describes the statistical behavior of an out-of-equilibrium system in terms of various scattering processes considering their specific scattering rates. The transport distribution function is defined as

$$\sigma(\varepsilon, T) = \int \sum_b \mathbf{v}_{b,\mathbf{k}} \times \mathbf{v}_{b,\mathbf{k}} \tau_{b,\mathbf{k}} \delta(\varepsilon - \varepsilon_{b,\mathbf{k}}) \frac{d\mathbf{k}}{8\pi^3} \tag{10}$$

where b is the band index, $\mathbf{k}$ the conserved wavevector, $\mathbf{v}_{b,\mathbf{k}}$ the carrier velocities, $\boldsymbol{\tau}_{b,\mathbf{k}}$ the relaxation time, and $\varepsilon_{b,\mathbf{k}}$ the band

energies. $\sigma(\varepsilon, T)$ can be used to compute the moments of the generalized transport coefficients

$$L^\alpha = q^2 \int \sigma(\varepsilon, T)(\varepsilon - \mu)^\alpha \left(-\frac{\partial f_F(\varepsilon; \mu, T)}{\partial \varepsilon} \right) d\varepsilon \tag{11}$$

with f_F the Fermi distribution and μ the chemical potential, that, in turn, are used to access the electronic transport coefficients of interest, namely the electrical conductivity σ and the electronic thermal conductivity κ_e, as

$$\sigma = L^{(0)} \tag{12}$$

$$\kappa_e = \frac{1}{q^2 T} \left[\frac{(L^{(1)})^2}{L^{(0)}} - L^{(2)} \right] \tag{13}$$

The integration of the BTE requires an accurate description of the electronic band structure. BoltzTraP2 code[30] provides such a description using an interpolation method based on a Fourier expansion that takes as input the electronic energies for different k-points, previously calculated by a DFT code (see Figure 6a). The code then computes the Fermi integrals for different temperatures and Fermi levels, and returns as output all of the transport coefficients.[29,30] In this work, calculations are performed at zero doping.

The relaxation time $\boldsymbol{\tau}_{b,\mathbf{k}}$ typically depends on the temperature T and on the charge carrier energy ε. All scattering events that can influence electron conduction, such as impurity scattering, phonon scattering, *etc.*, are summed in this parameter according to the Matthiessen law.[60] In many cases, as a first approximation, the relaxation time is often assumed to be constant. Within the constant relaxation time approximation (CRTA), quantities such as $\sigma_0 = \sigma/\tau_0$ and $\kappa_0 = \kappa/\tau_0$ are determined by the band structure where the temperature dependence exclusively comes from the electronic occupation function. This approach is quite efficient in terms of the computational time and globally provides good quantitative agreement with experimental measurements for lightly doped semiconductors,[61] where charge carriers are concentrated in specific bands and wave vectors. However, for highly doped semiconductors and metals, charge carriers are located at various places (various bands b and wave vectors $\mathbf{k}$) and the electronic relaxation time thus varies significantly on the Fermi surface.[62] In these particular cases, the CRTA has shown limitations and more advanced computational theories or models must be considered.

To obtain a good description of the electronic properties of metallic systems, both the temperature and energy dependences $\tau_{b,\mathbf{k}}$ must be considered in eq 10. The temperature- and energy dependence is dictated by the scattering mechanisms. The most important mechanisms of electron scattering in metals are (i) defects and charged impurity scattering, dominant at low temperatures (<100 K) and (ii) electron–phonon scattering, dominant at high temperatures. An analytical model expression for $\tau(T, \varepsilon)$, developed on the basis of known semiclassical theories, can be formulated as[63,64]

$$\tau(T, \varepsilon) = \tau_{ref} \left(\frac{T}{T_{ref}} \right)^\gamma \left(\frac{\varepsilon}{\varepsilon_{ref}} \right)^{\lambda - 1/2} \tag{14}$$

where τ_{ref} is a suitable reference value of τ at a temperature T_{ref} and ε_{ref} is the bottom of the conduction band. At low temperatures, γ and λ exponents in eq 14 are, respectively, 0 and 2, reflecting the effect of defects and impurities. At high
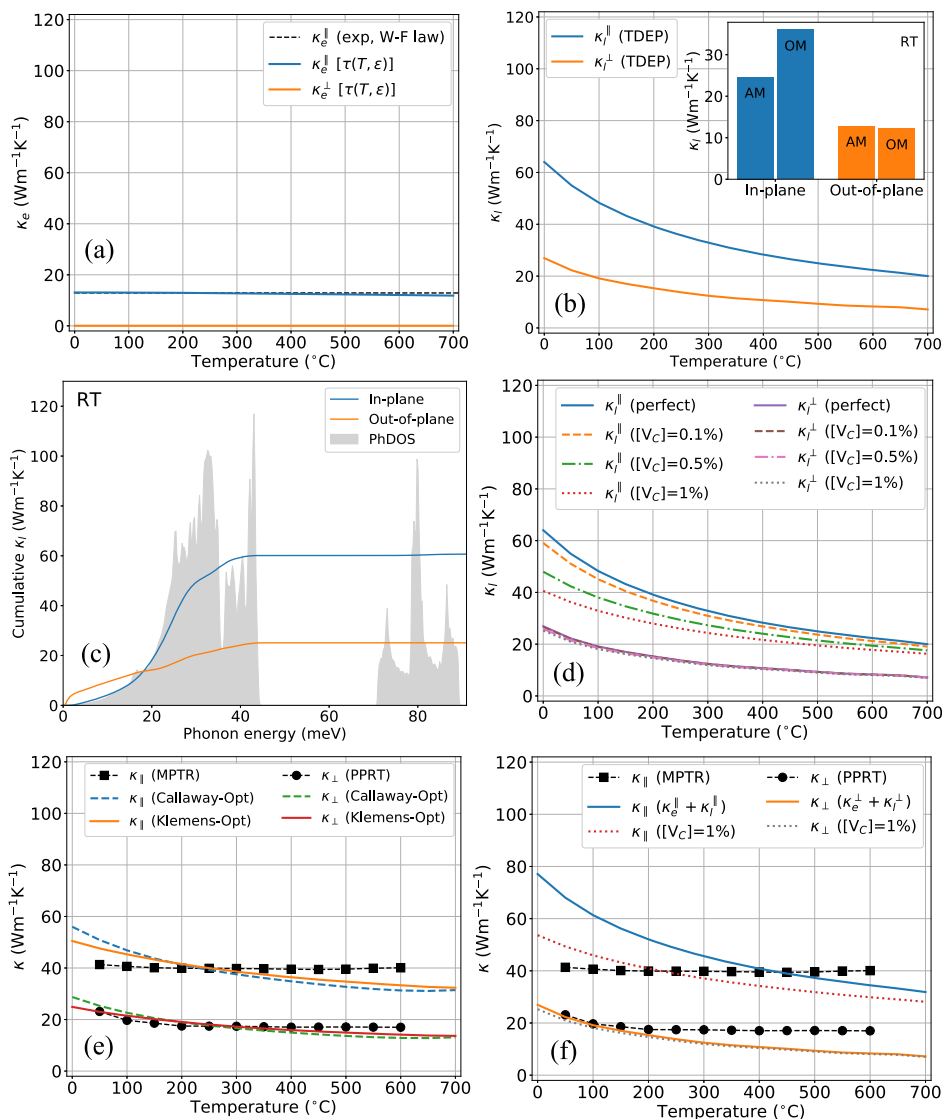
Figure 5. (a) In-plane κ_e extracted from the Wiedemann−Franz law considering the experimental electrical resistivity $\rho_\parallel(T)$ from Figure 3a and κ_e computed with $\tau(T, \varepsilon)$ defined in eq 15, (b) κ_l computed with anharmonic phonon−phonon scattering processes, with the contribution from optical and acoustic modes (OM and AM, respectively) at RT shown in the inset, (c) cumulative lattice thermal conductivity at RT, (d) κ_l for various concentrations of C vacancies, (e) κ obtained as the sum of κ_e and the predicted κ_l from Callaway and Klemens models, and (f) total computed thermal conductivity compared to the experimental curves obtained in this work.
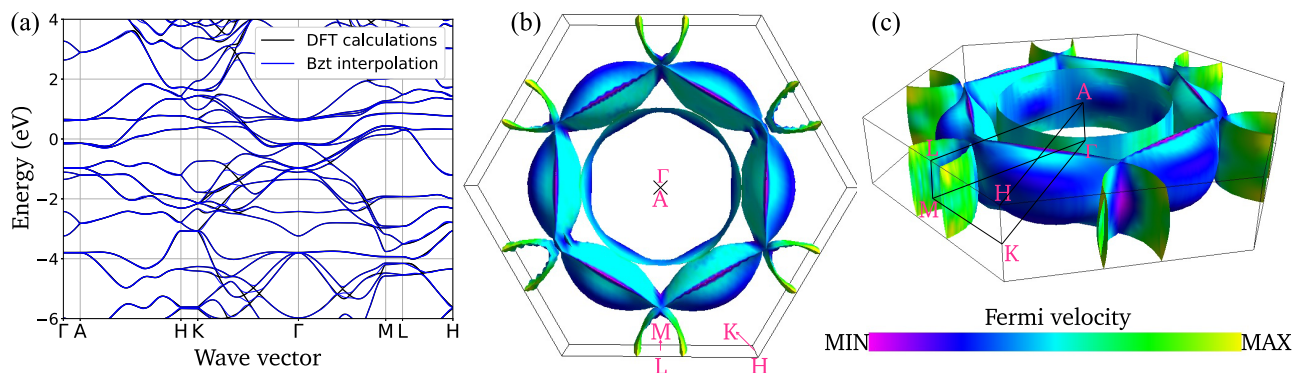

Figure 6. First-principles (a) electronic band structure of Cr$_2$AlC, with the Fermi level fixed as the reference of zero energy and (b, c) Fermi surfaces computed using the Fermisurfer code[50] and color coded depending on Fermi velocities.

temperatures, γ and λ exponents are, respectively, equal to −1 and 0 and the linear temperature dependence T^{-1} of the

relaxation time reflects the dominance of electron−phonon scattering mechanisms. Given that we are interested in the 0−

700 °C temperature range for which the relaxation time is governed by electron−phonon scattering processes, the expression of the relaxation time is given by

$$\tau(T, \, \varepsilon) = \tau_{ref}\left(\frac{T}{T_{ref}}\right)^{-1}\left(\frac{\varepsilon}{\varepsilon_{ref}}\right)^{-1/2} \tag{15}$$

where ε_{ref} is taken as the Fermi energy for a metallic system. The T^{-1} dependence in the model relaxation time allows recovery of the linear temperature dependence of $\rho_{\parallel}(T)$ in Figure 3a. A value of $\tau_{ref} = 5$ fs at $T_{ref} = 273$ K is chosen to fit the experimental in-plane resistivity curve in Figure 3a and is in good agreement with the recently determined electronic relaxation times in Cr_2AlC single crystals.[65] Similarly, a value of $\tau_{ref} = 0.06$ fs at $T_{ref} = 273$ K is chosen to match the out-of-plane resistivity value of 1.5×10^{-4} Ωm at 273 K (see Figure 3b).[25] Since no experimental data is available for $\rho_{\perp}$ above 273 K, the only indication used to extract a physical relaxation time is the anisotropy ratio of ∼300 observed for the resistivity at 273 K.[25] The temperature- and energy-dependent relaxation time has been implemented in the BoltzTraP2 code and is used to investigate the electrical and thermal transport in Cr_2AlC single crystals.

In Figure 5a, $\kappa_e^{\parallel}$ and $\kappa_e^{\perp}$ are reported using the temperature- and energy-dependent relaxation time defined in eq 15. A value of 13 Wm^{-1} K^{-1} (0.04 Wm^{-1} K^{-1}) at RT for the in-plane (out-of-plane) direction is obtained and remains quasi-constant in the whole temperature range.

3.2.3. Lattice Thermal Conductivity. The lattice thermal conductivity κ_l of a perfect harmonic crystal is infinite and not a function of temperature. The lattice thermal resistance is dictated by phonon scattering processes that can be intrinsic, through anharmonic phonon−phonon scattering, or extrinsic, induced by isotopic disorder, point defects, or edge effects. The treatment of these scattering processes is mandatory to obtain a good description and temperature dependence of thermal and thermodynamic properties, especially at high temperatures.

3.2.3.1. Phonon Boltzmann Transport Equation. When a material is at equilibrium at the temperature T, the equilibrium phonon population $\overline{n}_{\nu}$ describes the number of phonons for each vibrational mode ν found at energy $\hbar\omega_{\nu}$. If a gradient of the temperature is applied, the phonon population deviates from its equilibrium condition and reaches an out-of-equilibrium condition.[66]

The first microscopic description of the lattice thermal conductivity was formulated in 1929 by Peierls,[67] and is nowadays known as the phonon BTE. This equation describes how the perturbation due to a gradient of the temperature involves a change in the phonon population due to all possible scattering mechanisms. To accurately predict the thermal transport properties, an accurate description of the equilibrium and perturbed phonon populations is required, as well as of their interactions and lifetimes.[66] In practice, the harmonic quantities, such as phonon frequencies, group velocities, and phonon populations, can be obtained *ab initio* by computing the second-order IFC using DFPT. The challenge thus resides in the determination of the anharmonic quantities, such as phonon scattering rates and linewidths. The total out-of-equilibrium distribution n_{ν} in its linearized form is given by

$$n_{\nu} = \overline{n}_{\nu}(\overline{n}_{\nu} + 1)F_{\nu}\nabla T \tag{16}$$

where F_{ν} corresponds to the deviation of the phonon population with respect to the equilibrium condition. The computation of n_{ν}, which is the key quantity to be evaluated, requires to solve the linearized BTE for phonons

$$c_{\nu}\nabla T\frac{\partial\overline{n}_{\nu}}{\partial T} = \sum_{\nu'}\Omega_{\nu,\nu'}n_{\nu'} \tag{17}$$

where $\Omega_{\nu,\nu'}$ is a matrix of scattering rates acting on the phonon population. The lattice thermal conductivity can be expressed as

$$\kappa_l = \frac{\hbar^2}{\Omega k_B T^2}\sum_{\nu}\overline{n}_{\nu}(\overline{n}_{\nu} + 1)c_{\nu}\omega_{\nu}F_{\nu} \tag{18}$$

where Ω is the unit cell volume, ω_{ν} the phonon frequencies, and c_{ν} the corresponding group velocities. Additional information on the computation of the lattice thermal conductivity can be found in ref 66.

In most cases, phonons are treated individually through the single-mode approximation (SMA).[68−70] This relies on the assumption that heat current is dissipated every time a phonon undergoes a scattering event,[71] and approximates F_{ν} with $c_{\nu}\,\omega_{\nu}\,\tau_{\nu}$, where τ_{ν} is the relaxation time of the phonon mode ν. While the SMA properly describes the depopulation of a phonon mode after any scattering process, the repopulation process is usually poorly described due to a loss of memory of the initial phonon distribution (final states are repopulated isothermally).[71,72] In particular, the SMA has shown some limitations in accurately describing the lattice thermal conductivity in layered compounds and two-dimensional systems.[71]

Recently, Hellman et al.[31−33] proposed a formalism to obtain the third-order IFCs and to accurately calculate the lattice thermal conductivity from the iterative solution of the phonon BTE. The first step consists in computing the second- and third-order force constant matrices that are both temperature- and volume-dependent. For this purpose, an ensemble of 30 noncorrelated configurations generated from a Gaussian distribution of harmonic input phonons is used to sample the Born−Oppenheimer potential energy surface at a finite temperature. Then, a minimization scheme between the forces model and the *ab initio* computed forces is used, and leads to the direct determination of the force constant matrices. The second step consists in iteratively solving the phonon Boltzmann equation in eq 18, starting from an initial guess F_{ν}^0 to obtain the nonequilibrium distribution.

Figure 5b presents the computed lattice thermal conductivities in-plane $\kappa^{\parallel}$ and out-of-plane $\kappa_l^{\perp}$ for Cr_2AlC single crystals, when only anharmonic phonon−phonon scattering processes are considered. The inclusion of isotopic scattering processes does not modify the lattice thermal conductivity, as expected from the small natural isotopic diversity of Cr, Al, and C elements. Grain boundary scattering processes can play an important role in phonon transport as polycrystallinity tends to drastically decrease the lattice thermal conductivity.[73] However, in the present work, there is no reason to include these scattering processes since all measurements are performed on single crystals with a single grain of a few cm^2. Phonon scattering from point defects can also play an important role in limiting the thermal conductivity. Since both experimental and theoretical studies gave evidence for significant amounts of vacancies in MAX phases,[2,74] these defects are taken into account in the computation of the lattice thermal conductivity.

A vacancy can be regarded as a perturbation of the crystal corresponding to the removal of the mass of one atom and the force constants of two atoms.[75] Hence, the energy associated with a vacancy can be treated as equivalent to an isotopic defect corresponding to a change of mass $\Delta M = -3M$, where M is the atomic mass of the missing atom,[75] i.e., the C atom in Cr_2AlC.[74] Concentrations of C vacancies ranging from 0.1 to 1% are considered. The results are presented in Figure 5d. While $\kappa_l^{\perp}$ remains almost constant over the whole temperature range, $\kappa_l^{\parallel}$ is reduced, especially in the 0−300 °C temperature range by the inclusion of C vacancies. This can be understood from the analysis of the high-energy phonon branches, shown in Figure 7 and detailed in ref 28. In fact, the presence or the
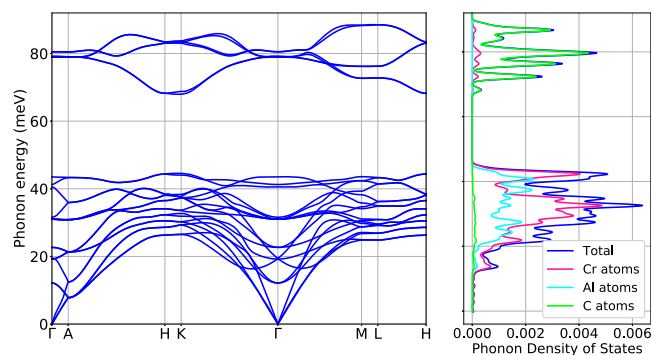

Figure 7. First-principles phonon spectrum of Cr_2AlC along major crystallographic directions with the projected phonon density of states.[28]

absence of C atoms only affects the in-plane phonon propagation and lattice thermal conductivity since, for the high-energy C-related modes, there is no phonon propagation feasible perpendicular to the plane, due to the flatness of the bands.

3.2.3.2. Callaway and Klemens Models. An efficient alternative to the phonon BTE to compute the lattice thermal conductivity is the Debye−Callaway model (detailed in the Supporting Information). Considering the optimized values for the parameters used in the model, both the in-plane and the out-of-plane lattice thermal conductivities are computed and the total thermal conductivities, including the electronic contributions, are presented (dashed lines) in Figure 5e. The agreement for both $\kappa_{\parallel}$ and $\kappa_{\perp}$ with the experimental curves is quite good.

Using the Klemens model (detailed in the Supporting Information) and optimizing at the same time both the effects of umklapp processes and defects lead to the curves (solid lines) presented in Figure 5e. The agreement with the experimental curves is good and is slightly improved with respect to the Callaway model, especially around RT.

4. DISCUSSION

In Figure 4a, the experimental measurements of the heat capacity of Cr_2AlC are slightly different from the values reported by Tian et al.[52] However, the theoretical total heat capacity reproduces the experimental data with very good accuracy, inducing a high confidence in the measurement techniques used. In addition, such agreement allows us to state that the AM contribution is clearly the dominant one, while the electronic, anharmonic, and OM contributions are similar

in magnitude and remain low compared to the AM contribution.

A linear temperature dependence of the electrical resistivity is observed in Figure 3a, as is usual in metals, due to the linear increase of the phonon occupation with temperature. Not surprisingly, the Wiedemann−Franz law gives a good approximation of the electronic thermal conductivity, and leads to results similar to those obtained with the BoltzTraP2 code using a temperature-dependent relaxation time (see Figure 5a). The large anisotropy observed in the electrical resistivities,[25] with an out-of-plane resistivity about 300 times higher than the in-plane one, leads to a negligible electronic contribution to the out-of-plane thermal conductivity. This anisotropy in the electronic transport can also be noticed from the electronic band structure and Fermi surface, as shown in Figure 6. The open tubular structure of the Fermi surface depicted in Figure 6b,c suggests a quasi two-dimensional character of the Cr_2AlC system, in agreement with the results from Ito et al.[27] Moreover, from eq 10, it is clear that carrier velocities, which are linked to the band dispersion, play an important role in the electronic transport. As a consequence, in Figure 6a, the dispersive bands along directions parallel to the plane (i.e., A−H, Γ−K, Γ−M, L−H) will lead to high carrier velocities and good electronic conductivity in the plane, while the almost flat bands along directions perpendicular to the plane (i.e., Γ−A, H−K, M−L) explain the weak out-of-plane conductivity. This is confirmed by the evaluation of the carrier velocities at the Fermi surface (see Figure 6b,c) for which the in-plane component is higher than the out-of-plane one (not shown).

The results for the lattice thermal conductivity computed with the TDEP code, considering anharmonic phonon−phonon scattering processes, are shown in Figure 5b. Both in-plane and out-of-plane κ_l decrease with the temperature, which is a signature of umklapp-dominated scattering processes. Although Cr_2AlC has relatively isotropic sound velocities (see Table 1),[28] it has a significantly anisotropic lattice thermal conductivity. This can be explained by the cumulative κ_l depicted in Figure 5c, where the anisotropy clearly starts at energies greater than 20 meV, mostly corresponding to optical modes. The low-lying optical branches—with the energy below 40 meV—in the phonon spectrum of Cr_2AlC (see Figure 7) are very dispersive, with higher group velocities in the ab-plane (along Γ−K and Γ−M) than along the c-axis (along Γ−A). Consequently, the optical modes significantly contribute to κ_l, particularly for the in-plane direction as shown in the inset of Figure 5b. This decomposition partly explains the intrinsic anisotropy present in the MAX phases, in general, and in Cr_2AlC, in particular. A good qualitative and quantitative agreement with the experimental thermal conductivity can be reached by considering both Callaway and Klemens models for the computation of κ_l, with optimized parameters, as highlighted in Figure 5e.

The computed total thermal conductivities are presented in Figure 5f and both slightly decrease with the temperature. An anisotropy ratio slightly higher than 2 is predicted over the whole temperature range. A comparison with the experimental data is also provided in Figure 5f. A qualitative agreement is found between the experimental and computed thermal conductivity curves, with an overestimation of the experimental $\kappa_{\parallel}$ by 65% and an underestimation of the experimental $\kappa_{\perp}$ by 4% at 50 °C. The overestimation of $\kappa_{\parallel}$ can be due to

various electron/phonon scattering sources and intrinsic structural defects present in the samples and not considered in the calculations. For example, it is shown in Figure 5d that the inclusion of C vacancies in our model reduces $\kappa_l^{\|}$ in the 0–300 °C temperature range, while keeping $\kappa_l^{\perp}$ constant. Consequently, the deviation between the calculated and experimental in-plane thermal conductivities at 50 °C goes down to 55 and 19% considering scattering processes with C vacancies, with concentrations of 0.1 and 1%, respectively. This confirms that the overestimation of the in-plane thermal conductivity can be explained by the missing scattering processes in the calculations, which can play an important role especially around the RT.

Interestingly, while the calculations predict a decreasing behavior for the thermal conductivity with the temperature—as intuitively deduced from the decrease of the phonon lifetimes with T—the experimental curves exhibit two different trends. For the in-plane thermal conductivity, some curves decrease with T while others increase with T, leading to an average curve that is almost constant on the whole temperature range. For the out-of-plane thermal conductivity, the curve slightly decreases before saturation above 200 °C. It seems that something, which is not caught by our simulations, maintains the thermal current constant even at a higher temperature. This could be linked to a possible thermal expansion with the increasing T or with a potential annealing of the sample at a higher T, reducing the number of defects in it. More work is needed to clarify this situation, which will be the scope of our future research.

In the present work, the main result is the quantitative analysis of the anisotropy in the thermal conductivity of Cr_2AlC single crystals confirmed by both experimental and theoretical approaches. This anisotropy arises from both the electronic and lattice contributions, the latter being the dominant term. At RT, the lattice contribution represents ~81% of the total in-plane thermal conductivity and decreases with T to reach 63% at 600 °C. For the out-of-plane thermal conductivity, the electronic contribution is almost zero and the thermal transport is only feasible through lattice vibrations. Interestingly, the anisotropy ratio of 300 observed in the electronic transport is now reduced down to ~2 for the thermal transport, as a consequence of the lattice vibrations, which play an important role along both in-plane and out-of-plane directions.

5. CONCLUSIONS

In summary, the heat capacity of Cr_2AlC single crystals is measured and accurately reproduced using simple analytic models. The contribution from acoustic phonon modes is clearly the dominant one, while the electronic, anharmonic, and optical modes' contributions represent together at most 25% of the heat capacity.

The in-plane and out-of-plane thermal conductivities of Cr_2AlC single crystals are measured using various experimental techniques and compared to *ab initio* calculations. An accurate microscopic description of heat transport is achieved and the electronic contribution to thermal conductivity is determined using a temperature-dependent electronic relaxation time. Solving iteratively the BTE for phonons, the lattice thermal conductivity is estimated. Additionally, Callaway and Klemens models provide a qualitative and quantitative description of the lattice thermal conductivity. Both in-plane and out-of-plane thermal conductivities computed *ab initio* are in good

agreement with the present experiments and with previously reported experimental data. For the out-of-plane thermal conductivity, the quantitative agreement is also correct in the entire temperature range. Regarding the in-plane thermal conductivity, the computed data slightly overestimate the experimental ones below 400 °C, whereas they underestimate them at higher temperatures. The inclusion of scattering processes by C vacancies improves the prediction of $\kappa_{\|}$, especially between RT and 300 °C, and leads to a good quantitative agreement with the experimental curve. The remaining deviation between calculated and experimental thermal conductivities can possibly be assigned to additional scattering phenomena, present in real samples, and not considered in this work. Besides, the saturation behavior of the experimental curves at high temperatures is not caught by our simulations. It could be linked to a possible thermal expansion or annealing of the sample with increasing T. More investigation is needed to shed light on this interesting point.

As a main conclusion, the anisotropy reported experimentally is accurately reproduced theoretically and seems to mainly arise from the lattice contribution. A similar anisotropy in the transport properties is expected for other MAX phases with identical layered structures. Consequently, we believe that this first-principles approach can be effectively applied to investigate the thermal conductivities of other layered systems. From an applicative aspect, accurately predicting and describing the anisotropic thermal conductivity in layered systems is essential for device engineering, especially for energy dissipation in electronics and high-temperature applications.

■ ASSOCIATED CONTENT

Ⓢ Supporting Information

The Supporting Information is available free of charge at https://pubs.acs.org/doi/10.1021/acs.jpcc.0c08384.

> Analytical models (*i.e.*, Callaway and Klemens) for the computation of the lattice thermal conductivity (PDF)

■ AUTHOR INFORMATION

Corresponding Author

A. Champagne − *Institute of Condensed Matter and Nanosciences, Université catholique de Louvain, B-1348 Louvain-la-Neuve, Belgium;* ⓘ orcid.org/0000-0002-6013-2887; Email: aurelie.champagne@uclouvain.be

Authors

J.-L. Battaglia − *I2M Laboratory, UMR CNRS 5295, University of Bordeaux, 33405 Talence, France*

T. Ouisse − *Université Grenoble Alpes, CNRS, Grenoble INP, LMGP, F-38000 Grenoble, France*

F. Ricci − *Institute of Condensed Matter and Nanosciences, Université catholique de Louvain, B-1348 Louvain-la-Neuve, Belgium;* ⓘ orcid.org/0000-0002-2677-7227

A. Kusiak − *I2M Laboratory, UMR CNRS 5295, University of Bordeaux, 33405 Talence, France*

C. Pradere − *I2M Laboratory, UMR CNRS 5295, University of Bordeaux, 33405 Talence, France*

V. Natu − *Department of Materials Science and Engineering, Drexel University, Philadelphia, Pennsylvania 19104, United States*

A. Dewandre − *CESAM-QMAT-nanomat, and European Theoretical Spectroscopy Facility, Université de Liège, B-4000 Sart-Tilman, Belgium*

M. J. Verstraete − *CESAM-QMAT-nanomat, and European Theoretical Spectroscopy Facility, Université de Liège, B-4000 Sart-Tilman, Belgium*

M. W. Barsoum − *Department of Materials Science and Engineering, Drexel University, Philadelphia, Pennsylvania 19104, United States;* ◉ orcid.org/0000-0001-7800-3517

J.-C. Charlier − *Institute of Condensed Matter and Nanosciences, Université catholique de Louvain, B-1348 Louvain-la-Neuve, Belgium*

Complete contact information is available at:
https://pubs.acs.org/10.1021/acs.jpcc.0c08384

Notes
The authors declare no competing financial interest.

REFERENCES

(1) Barsoum, M. W. The $M_{n+1}AX_n$ phases: A new class of solids: Thermodynamically stable nanolaminates. *Prog. Solid State Chem.* 2000, 28, 201−281.

(2) Sokol, M.; Natu, V.; Kota, S.; Barsoum, M. W. On the chemical diversity of the MAX phases. *Trends Chem.* 2019, 1, 210−223.

(3) Liu, Z.; Wu, E.; Wang, J.; Qian, Y.; Xiang, H.; Li, X.; Jin, Q.; Sun, G.; Chen, X.; Wang, J.; et al. Crystal structure and formation mechanism of $(Cr_{2/3}Ti_{1/3})_3AlC_2$ MAX phase. *Acta Mater.* 2014, 73, 186−193.

(4) Tao, Q.; Dahlqvist, M.; Lu, J.; Kota, S.; Meshkian, R.; Halim, J.; Palisaitis, J.; Hultman, L.; Barsoum, M. W.; Persson, P. O.; et al. Two-dimensional $Mo_{1.33}C$ MXene with divacancy ordering prepared from parent 3D laminate with in-plane chemical ordering. *Nat. Commun.* 2017, 8, No. 14949.

(5) Dahlqvist, M.; Lu, J.; Meshkian, R.; Tao, Q.; Hultman, L.; Rosen, J. Prediction and synthesis of a family of atomic laminate phases with Kagomé-like and in-plane chemical ordering. *Sci. Adv.* 2017, 3, No. e1700642.

(6) Tao, Q.; Ouisse, T.; Pinek, D.; Chaix-Pluchery, O.; Wilhelm, F.; Rogalev, A.; Opagiste, C.; Jouffret, L.; Champagne, A.; Charlier, J.-C.; et al. Rare-earth (RE) nanolaminates $Mo_4RE_4Al_7C_3$ featuring ferromagnetism and mixed-valence states. *Phys. Rev. Mater.* 2018, 2, No. 114401.

(7) Tao, Q.; Lu, J.; Dahlqvist, M.; Mockute, A.; Calder, S.; Petruhins, A.; Meshkian, R.; Rivin, O.; Potashnikov, D.; Caspi, E.; et al. Atomically layered and ordered rare-earth i-MAX phases: A new class of magnetic quaternary compounds. *Chem. Mater.* 2019, 31, 2476−2485.

(8) Petruhins, A.; Lu, J.; Hultman, L.; Rosen, J. Synthesis of atomically layered and chemically ordered rare-earth (RE) i-MAX phases; $(Mo_{2/3}RE_{1/3})_2GaC$ with RE = Gd, Tb, Dy, Ho, Er, Tm, Yb, and Lu. *Mater. Res. Lett.* 2019, 7, 446−452.

(9) Barsoum, M. W. *MAX Phases*, 1st ed.; Wiley-Blackwell, 2013.

(10) Barsoum, M. W.; El-Raghy, T. The MAX phases: Unique new carbide and nitride materials. *Am. Sci.* 2001, 89, 334.

(11) Nelson, M.; Agne, M. T.; Anasori, B.; Yang, J.; Barsoum, M. W. Synthesis and characterization of the mechanical properties of Ti_3SiC_2/Mg and Cr_2AlC/Mg alloy composites. *Mater. Sci. Eng., A* 2017, 705, 182−188.

(12) Gruber, J.; Lang, A. C.; Griggs, J.; Taheri, M. L.; Tucker, G. J.; Barsoum, M. W. Evidence for bulk ripplocations in layered solids. *Sci. Rep.* 2016, 6, No. 33451.

(13) Griggs, J.; Lang, A. C.; Gruber, J.; Tucker, G.; Taheri, M.; Barsoum, M. Spherical nanoindentation, modeling and transmission electron microscopy evidence for ripplocations in Ti_3SiC_2. *Acta Mater.* 2017, 131, 141−155.

(14) Barsoum, M.; Tucker, G. Deformation of layered solids: Ripplocations not basal dislocations. *Scr. Mater.* 2017, 139, 166−172.

(15) Barsoum, M. W.; Zhao, X.; Shanazarov, S.; Romanchuk, A.; Koumlis, S.; Pagano, S. J.; Lamberson, L.; Tucker, G. J. Ripplocations: A universal deformation mechanism in layered solids. *Phys. Rev. Mater.* 2019, 3, No. 013602.

(16) Badr, H. O.; Champagne, A.; Ouisse, T.; Charlier, J.-C.; Barsoum, M. W. Elastic properties and hardness values of V_2AlC and Cr_2AlC single crystals. *Phys. Rev. Mater.* 2020, 4, No. 083605.

(17) Naguib, M.; Kurtoglu, M.; Presser, V.; Lu, J.; Niu, J.; Heon, M.; Hultman, L.; Gogotsi, Y.; Barsoum, M. W. Two-dimensional nanocrystals produced by exfoliation of Ti_3AlC_2. *Adv. Mater.* 2011, 23, 4248−4253.

(18) Barsoum, M. W.; El-Raghy, T. Synthesis and characterization of a remarkable ceramic: Ti_3SiC_2. *J. Am. Ceram. Soc.* 1996, 79, 1953−1956.

(19) Drulis, M. K.; Drulis, H.; Gupta, S.; Barsoum, M. W.; El-Raghy, T. On the heat capacities of M_2AlC (M=Ti,V,Cr) ternary carbides. *J. Appl. Phys.* 2006, 99, No. 093502.

(20) Hettinger, J. D.; Lofland, S. E.; Finkel, P.; Meehan, T.; Palma, J.; Harrell, K.; Gupta, S.; Ganguly, A.; El-Raghy, T.; Barsoum, M. W. Electrical transport, thermal transport, and elastic properties of M_2AlC (M = Ti, Cr, Nb, and V). *Phys. Rev. B* 2005, 72, No. 115120.

(21) Mercier, F.; Ouisse, T.; Chaussende, D. Morphological instabilities induced by foreign particles and Ehrlich-Schwoebel effect during the two-dimensional growth of crystalline Ti_3SiC_2. *Phys. Rev. B* 2011, 83, No. 075411.

(22) Mercier, F.; Chaix-Pluchery, O.; Ouisse, T.; Chaussende, D. Raman scattering from Ti_3SiC_2 single crystals. *Appl. Phys. Lett.* 2011, 98, No. 081912.

(23) Ouisse, T.; Sarigiannidou, E.; Chaix-Pluchery, O.; Roussel, H.; Doisneau, B.; Chaussende, D. High temperature solution growth and characterization of Cr_2AlC single crystals. *J. Cryst. Growth* 2013, 384, 88−95.

(24) Shi, L.; Ouisse, T.; Sarigiannidou, E.; Chaix-Pluchery, O.; Roussel, H.; Chaussende, D.; Hackens, B. Synthesis of single crystals of V_2AlC phase by high-temperature solution growth and slow cooling technique. *Acta Mater.* 2015, 83, 304−309.

(25) Ouisse, T.; Shi, L.; Piot, B. A.; Hackens, B.; Mauchamp, V.; Chaussende, D. Magnetotransport properties of nearly-free electrons in two-dimensional hexagonal metals and application to the $M_{n+1}AX_n$ phases. *Phys. Rev. B* 2015, 92, No. 045133.

(26) Ouisse, T.; Barsoum, M. W. Magnetotransport in the MAX phases and their 2D derivatives: MXenes. *Mater. Res. Lett.* **2017**, *5*, 365−378.

(27) Ito, T.; Pinek, D.; Fujita, T.; Nakatake, M.; Ideta, S.-i.; Tanaka, K.; Ouisse, T. Electronic structure of Cr_2AlC as observed by angle-resolved photoemission spectroscopy. *Phys. Rev. B* **2017**, *96*, No. 195168.

(28) Champagne, A.; Bourdarot, F.; Bourges, P.; Piekarz, P.; Pinek, D.; Gélard, I.; Charlier, J.-C.; Ouisse, T. Phonon dispersion curves in Cr_2AlC single-crystals. *Mater. Res. Lett.* **2018**, *6*, 378−383.

(29) Madsen, G. K.; Singh, D. J. BoltzTraP. A code for calculating band-structure dependent quantities. *Comput. Phys. Commun.* **2006**, *175*, 67−71.

(30) Madsen, G. K.; Carrete, J.; Verstraete, M. J. BoltzTraP2, a program for interpolating band structures and calculating semi-classical transport coefficients. *Comput. Phys. Commun.* **2018**, *231*, 140−145.

(31) Hellman, O.; Abrikosov, I. A.; Simak, S. I. Lattice dynamics of anharmonic solids from first principles. *Phys. Rev. B* **2011**, *84*, No. 180301.

(32) Hellman, O.; Steneteg, P.; Abrikosov, I. A.; Simak, S. I. Temperature dependent effective potential method for accurate free energy calculations of solids. *Phys. Rev. B* **2013**, *87*, No. 104111.

(33) Hellman, O.; Abrikosov, I. A. Temperature-dependent effective third-order interatomic force constants from first principles. *Phys. Rev. B* **2013**, *88*, No. 144301.

(34) Swartzendruber, L. J. Correction factor tables for four-point probe resistivity measurements on thin, circular semiconductor samples. *Tech. Note* **1964**, *6*, 43.

(35) Kusiak, A.; Martan, J.; Battaglia, J.-L.; Daniel, R. Using pulsed and modulated photothermal radiometry to measure the thermal conductivity of thin films. *Thermochim. Acta* **2013**, *556*, 1−5.

(36) Gaverina, L.; Batsale, J. C.; Sommier, A.; Pradere, C. Pulsed flying spot with the logarithmic parabolas method for the estimation of in-plane thermal diffusivity fields on heterogeneous and anisotropic materials. *J. Appl. Phys.* **2017**, *121*, No. 115105.

(37) Ruffio, E.; Pradere, C.; Sommier, A.; Batsale, J.-C.; Kusiak, A.; Battaglia, J.-L. Signal noise ratio improvement technique for bulk thermal diffusivity measurement. *Int. J. Therm. Sci.* **2018**, *129*, 385−395.

(38) Hohenberg, P.; Kohn, W. Inhomogeneous Electron Gas. *Phys. Rev.* **1964**, *136*, B864−B871.

(39) Kohn, W.; Sham, L. J. Self-consistent equations including exchange and correlation effects. *Phys. Rev.* **1965**, *140*, A1133−A1138.

(40) Baroni, S.; Giannozzi, P.; Testa, A. Green's-function approach to linear response in solids. *Phys. Rev. Lett.* **1987**, *58*, No. 1861.

(41) Gonze, X. Perturbation expansion of variational principles at arbitrary order. *Phys. Rev. A* **1995**, *52*, 1086−1095.

(42) Gonze, X. First-principles responses of solids to atomic displacements and homogeneous electric fields: Implementation of a conjugate-gradient algorithm. *Phys. Rev. B* **1997**, *55*, 10337−10354.

(43) Gonze, X.; Lee, C. Dynamical matrices, Born effective charges, dielectric permittivity tensors, and interatomic force constants from density-functional perturbation theory. *Phys. Rev. B* **1997**, *55*, 10355−10368.

(44) Baroni, S.; de Gironcoli, S.; Dal Corso, A.; Giannozzi, P. Phonons and related crystal properties from density-functional perturbation theory. *Rev. Mod. Phys.* **2001**, *73*, 515−562.

(45) Gonze, X.; Beuken, J.-M.; Caracas, R.; Detraux, F.; Fuchs, M.; Rignanese, G.-M.; Sindic, L.; Verstraete, M.; Zerah, G.; Jollet, F.; et al. First-principles computation of material properties: the ABINIT software project. *Comput. Mater. Sci.* **2002**, *25*, 478−492.

(46) Gonze, X.; Rignanese, G.; Verstraete, M.; Betiken, J.; Pouillon, Y.; Caracas, R.; Jollet, F.; Torrent, M.; Zerah, G.; Mikami, M.; et al. A brief introduction to the ABINIT software package. *Z. Kernenerg.* **2005**, *220*, 558−562.

(47) Gonze, X.; Amadon, B.; Anglade, P.-M.; Beuken, J.-M.; Bottin, F.; Boulanger, P.; Bruneval, F.; Caliste, D.; Caracas, R.; Côté, M.;

(48) Perdew, J. P.; Burke, K.; Ernzerhof, M. Generalized gradient approximation made simple. *Phys. Rev. Lett.* **1996**, *77*, 3865−3868.

(49) Hamann, D. R. Optimized norm-conserving Vanderbilt pseudopotentials. *Phys. Rev. B* **2013**, *88*, No. 085117.

(50) Kawamura, M. FermiSurfer: Fermi-surface viewer providing multiple representation schemes. *Comput. Phys. Commun.* **2019**, *239*, 197−203.

(51) Ying, G.; He, X.; Li, M.; Du, S.; Han, W.; He, F. Effect of Cr_7C_3 on the mechanical, thermal, and electrical properties of Cr_2AlC. *J. Alloys Compd.* **2011**, *509*, 8022−8027.

(52) Tian, W.; Wang, P.; Zhang, G.; Kan, Y.; Li, Y.; Yan, D. Synthesis and thermal and electrical properties of bulk Cr_2AlC. *Scr. Mater.* **2006**, *54*, 841−846.

(53) Scabarozi, T.; Ganguly, A.; Hettinger, J. D.; Lofland, S. E.; Amini, S.; Finkel, P.; El-Raghy, T.; Barsoum, M. W. Electronic and thermal properties of $Ti_3Al(C_{0.5},N_{0.5})_2$, $Ti_2Al(C_{0.5},N_{0.5})$ and Ti_2AlN. *J. Appl. Phys.* **2008**, *104*, No. 073713.

(54) Manoun, B.; Gulve, R. P.; Saxena, S. K.; Gupta, S.; Barsoum, M. W.; Zha, C. S. Compression behavior of M_2AlC (M= Ti, V, Cr, Nb, and Ta) phases to above 50GPa. *Phys. Rev. B* **2006**, *73*, No. 024110.

(55) Sun, Z.; Ahuja, R.; Li, S.; Schneider, J. M. Structure and bulk modulus of M_2AlC (M = Ti, V, and Cr). *Appl. Phys. Lett.* **2003**, *83*, 899−901.

(56) Wang, J.; Wang, J.; Li, A.; Li, J.; Zhou, Y. Theoretical study on the mechanism of anisotropic thermal properties of Ti_2AlC and Cr_2AlC. *J. Am. Ceram. Soc.* **2014**, *97*, 1202−1208.

(57) Schneider, J. M.; Sigumonrong, D. P.; Music, D.; Walter, C.; Emmerlich, J.; Iskandar, R.; Mayer, J. Elastic properties of Cr_2AlC thin films probed by nanoindentation and ab initio molecular dynamics. *Scr. Mater.* **2007**, *57*, 1137−1140.

(58) Lofland, S. E.; Hettinger, J. D.; Harrell, K.; Finkel, P.; Gupta, S.; Barsoum, M. W.; Hug, G. Elastic and electronic properties of select M_2AX phases. *Appl. Phys. Lett.* **2004**, *84*, 508−510.

(59) Kota, S.; Agne, M.; Zapata-Solvas, E.; Dezellus, O.; Lopez, D.; Gardiola, B.; Radovic, M.; Barsoum, M. W. Elastic properties, thermal stability, and thermodynamic parameters of MoAlB. *Phys. Rev. B* **2017**, *95*, No. 144108.

(60) Dugdale, J. S.; Basinski, Z. S. Mathiessen's rule and anisotropic relaxation times. *Phys. Rev.* **1967**, *157*, 552−560.

(61) Ricci, F.; Chen, W.; Aydemir, U.; Snyder, G. J.; Rignanese, G.-M.; Jain, A.; Hautier, G. An ab initio electronic transport database for inorganic materials. *Sci. Data* **2017**, *4*, No. 170085.

(62) Mustafa, J. I.; Bernardi, M.; Neaton, J. B.; Louie, S. G. Ab initio electronic relaxation times and transport in noble metals. *Phys. Rev. B* **2016**, *94*, No. 155105.

(63) Delugas, P.; Filippetti, A.; Verstraete, M. J.; Pallecchi, I.; Marré, D.; Fiorentini, V. Doping-induced dimensional crossover and thermopower burst in Nb-doped $SrTiO_3$ superlattices. *Phys. Rev. B* **2013**, *88*, No. 045310.

(64) Farris, R.; Maccioni, M. B.; Filippetti, A.; Fiorentini, V. Influence of thermal conductivity and of non-constant relaxation time on thermoelectricity in Mg_3Sb_2. *J. Phys.: Conf. Ser.* **2019**, *1226*, No. 012010.

(65) Ouisse, T.; Pinek, D.; Barsoum, M. Modelling in-plane magneto-transport in Cr_2AlC. *Ceram. Int.* **2019**, *45*, 22956−22960.

(66) Fugallo, G.; Colombo, L. Calculating lattice thermal conductivity: a synopsis. *Phys. Scr.* **2018**, *93*, No. 043002.

(67) Peierls, R. Zur kinetischen Theorie der WÃd'meleitung in Kristallen. *Ann. Phys.* **1929**, *395*, 1055−1101.

(68) Klemens, P. Thermal conductivity and lattice vibrational modes. *Solid State Phys.* **1958**, *7*, 1−98.

(69) Callaway, J. Model for lattice thermal conductivity at low temperatures. *Phys. Rev.* **1959**, *113*, 1046−1051.

(70) Ziman, J. F. *Electrons and Phonons: The Theory of Transport Phenomena in Solids*; Oxford University Press, Oxford, 2001.

(71) Cepellotti, A.; Fugallo, G.; Paulatto, L.; Lazzeri, M.; Mauri, F.; Marzari, N. Phonon hydrodynamics in two-dimensional materials. *Nat. Commun.* **2015**, *6*, No. 6400.

(72) Fugallo, G.; Cepellotti, A.; Paulatto, L.; Lazzeri, M.; Marzari, N.; Mauri, F. Thermal conductivity of graphene and graphite: Collective excitations and mean free paths. *Nano Lett.* **2014**, *14*, 6109−6114.

(73) Maccioni, M. B.; Farris, R.; Fiorentini, V. Ab initio thermal conductivity of thermoelectric Mg_3Sb_2: Evidence for dominant extrinsic effects. *Phys. Rev. B* **2018**, *98*, No. 220301.

(74) Shah, S. H.; Bristowe, P. D. Point defect formation in M_2AlC (M = Zr, Cr) MAX phases and their tendency to disorder and amorphize. *Sci. Rep.* **2017**, *7*, No. 9667.

(75) Ratsifaritana, C. A.; Klemens, P. G. Scattering of phonons by vacancies. *Int. J. Thermophys.* **1987**, *8*, 737−750.